Baromagnetic Effect in Antiperovskite $Mn_3Ga_{0.95}N_{0.94}$ by Neutron Powder Diffraction Analysis

*Kewen Shi, Ying Sun, Jun Yan, Sihao Deng, Lei Wang, Hui Wu, Pengwei Hu, Huiqing Lu, Muhammad Imran Malik, Qingzhen Huang, and Cong Wang**

Strongly correlated materials have gained great interests in practical applications for their abundant properties.[1–3] In the strongly correlated systems, varying external field can affect multi-physical quantities simultaneously and induce interesting physical properties, such as magnetoelectric (ME) effect for Cr_2O_3[4] in magnetic or electric field, giant magnetocaloric effect (MCE) for $Gd_5Si_2Ge_2$,[5] $LaFe_{13−x}Si_x$-based alloys[6] and $MnFeP_{0.45}As_{0.55}$[7] in magnetic field. In particular, the applied external pressure field is an effective way to alter electronic structure, electronic density, magnetic structure, etc. of a material by changing the interatomic distances in its structure, which leads to important physical phenomena such as magnetic collapse,[8–10] metal–insulator transitions (MITs) in 3d transition-metal compounds,[11–13] valence fluctuations or Kondo-like characteristics in f-electron systems,[14,15] or the emergence of superconducting phases.[16,17] Many reports have revealed that the pressure is able to induce phase transitions including lattice, electronic, and magnetic phases for the strong spin-lattice coupling, and result in new pressure-induced physical properties, such as the barocaloric effect (BCE),[18–20] which has a potential application in solid-state refrigeration.

As a strong spin-lattice coupling system, antiperovskite compounds, Mn_3XN (where X represents transition metals and semiconducting elements), with a noncollinear magnetic ground state induced by the geometric frustration in the Mn_6N octahedron, are able to exhibit unique physical properties, such as abnormal thermal expansion,[21–24] unusual phase separation,[25] near zero temperature coefficient of resistivity,[26,27] magnetostriction,[28] and MCE.[29] Among those, Mn_3GaN with the triangular Γ^{5g} magnetic structure has attracted much attention due to its near zero thermal expansion and large negative thermal expansion behaviors, which were found to be related to the Γ^{5g} magnetic phase and the Γ^{5g}-paramagnetic (PM) transition, respectively.[30] Particularly, the giant BCE was reported in Mn_3GaN[31] and the piezomagnetic effect (without

magnetic phase transition) was also theoretically predicted in Mn_3GaN.[32] Therefore, it is expected that the pressure could induce large change of magnetic moment, as so-called baromagnetic effect (BME) (caused by magnetic phase transition due to an outer hydrostatic pressure). Unfortunately, to the best of our knowledge, so far there is no such a report on this property of Mn_3GaN. This particular property would have potential applications in ME devices and intelligent instruments. Therefore, it would be of great interest to study the baromagnetic effect in Mn_3GaN system and understand the origin of this effect.

In this work, we systematically study the changes of crystal and magnetic structures for antiperovskite compound $Mn_3Ga_{0.95}N_{0.94}$ by neutron powder diffraction (NPD) at different temperatures and pressure fields.[33] A new noncollinear magnetic structure was found in coexistence with the Γ^{5g} phase in $Mn_3Ga_{0.95}N_{0.94}$ at low temperature range of 6–50 K under atmospheric pressure, which has never been reported before. Remarkably, considerable BMEs correlated to the magnetic phase transitions induced by pressure field are for the first time observed in $Mn_3Ga_{0.95}N_{0.94}$. Our findings provide a new strategy to provoke magnetic effects by external fields.

The samples of a nominal composition Mn_3GaN were prepared by solid-state chemical reaction and the crystal structure (space group Pm-3m) and the magnetic structures are shown in **Figure 1**a–c determined by Rietveld refinement using neutron powder diffraction (NPD) data (see S1, Supporting Information). Mn_3GaN is paramagnetic (PM) at room temperature with the lattice constant of 3.88593(9) Å. The refinement results indicate that the occupancies of Mn [at 3c (0.5, 0.5, 0)], Ga [at 1a (0, 0, 0)] and N [at 2b (0.5, 0.5, 0.5)] are 1(fixed), 0.947(9) and 0.943(9), respectively. Therefore, the real composition of Mn_3GaN sample was defined to be $Mn_3Ga_{0.95}N_{0.94}$, which we thus use in the following. NPD experiments with temperature changes under atmospheric pressure were carried out to discern the structure evolution with temperature shown in Figure 1d. With decreasing temperature to 270 K, several magnetic peaks in the NPD pattern of $Mn_3Ga_{0.95}N_{0.94}$ begin to appear, which are confirmed to belong to the antiferromagnetic (AFM) phase by the refinement results and previous work[34] indicating a magnetic transition from PM to AFM at the Neel temperature of 272 K. The phase fraction of AFM phase reaches 100% at 150 K indicating the completion of the magnetic transition. The magnetic structure for the AFM phase shown in Figure 1b is corresponding to the rhombohedral (R-3) magnetic symmetry (Γ^{5g}) by refinement using NPD data at 150 K (see S1, Supporting Information). With temperature further cooling to 100 K, several new magnetic peaks appear, shown in Figure 1e, suggesting the occurrence of a

K. W. Shi, Dr. Y. Sun, Dr. J. Yan, S. H. Deng, Dr. L. Wang,
P. W. Hu, H. Q. Lu, M. I. Malik, Prof. C. Wang
Center for Condensed Matter and Materials
Department of Physics
Beihang University
Beijing 100191, P. R. China
E-mail: congwang@buaa.edu.cn
Dr. H. Wu, Dr. Q. Z. Huang
NIST Center for Neutron Research
National Institute of Standards and Technology
Gaithersburg, MD 20899-6102, USA

ADVANCED
MATERIALS
www.advmat.de
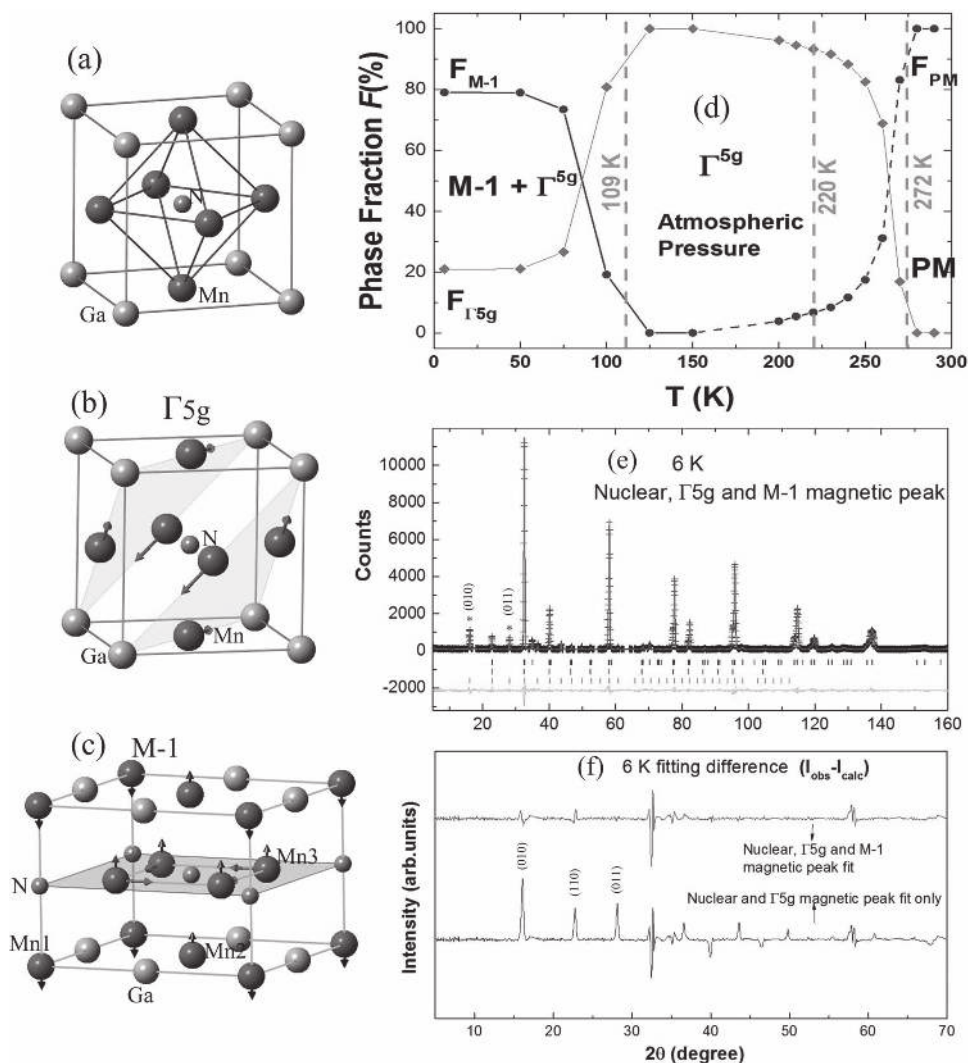
Materials
Views
www.MaterialsViews.com

Figure 1. a) Crystal structure, (b) Γ^{5g} magnetic structure, and (c) the new M-1 magnetic phase of $Mn_3Ga_{0.95}N_{0.94}$. d) Temperature dependence of the phase fraction for each phase in $Mn_3Ga_{0.95}N_{0.94}$ under atmospheric pressure. e) Nuclear, Γ^{5g} and M-1 magnetic peak fits at 6 K. The crosses show the experimental intensities (I_{obs}), the upper solid line shows the calculated intensities (I_{calc}), and the lower solid line is the difference between observed and calculated intensities ($I_{obs}-I_{calc}$). The vertical bars mark the angular positions of the nuclear (the first row, including peaks for MnO) and magnetic (Γ^{5g} at the second row and M-1 at the third row) Bragg peaks. The marked peaks are corresponding to the new magnetic peaks. f) The top solid line shows the difference ($I_{obs}-I_{calc}$) generated by nuclear, Γ^{5g} and M-1 magnetic fitting at 6 K. The bottom solid line shows the difference ($I_{obs}-I_{calc}$) generated by nuclear and Γ^{5g} magnetic fitting only at 6 K, so that the contributions by the M-1 magnetic structure are clearly visible.

new magnetic phase which has never been reported in Mn_3GaN system before. As shown in Figure 1c, the new magnetic structure with ferrimagnetic characteristic is labeled as M-1, which has a tetragonal (P 4) symmetry. Figure 1f shows the difference between the observed and calculated intensity ($I_{obs}-I_{calc}$) fitted by nuclear and Γ^{5g} structure, combined two magnetic structures (Γ^{5g} and M-1) with nuclear structure, respectively, at 6 K. From these curves, we can clearly identify the magnetic peaks for M-1 structure, while the magnetic peak (0.5, 0.5, 0), located at the position of nuclear (110) peak, stands for the ferromagnetic components in the M-1 magnetic structure for $Mn_3Ga_{0.95}N_{0.94}$. The refinement results indicate that the phase fraction of the M-1 magnetic phase remains 79% in the coexistence with the Γ^{5g} AFM phase at temperature range of 50–6 K. The lattice parameters for M-1 magnetic structure along x, y, and z axes are

$a_M = b_M = \sqrt{2}\,a$ and $c_M = a$ (a is the lattice parameter of the nuclear structure), respectively. The refinement results of the magnetic structure show that the Mn atoms have three different locations in this magnetic structure: Mn1 1a (0, 0, 0), Mn2 2b (0.5, 0.5, 0), Mn3 4d (0.25, 0.25, 0.5), as shown in Figure 1c. On the z = 0 plane, Mn1 and Mn2 atoms only have antiferromagnetic components alone z axis. The Mn3 atoms at the z = 0.5 plane have two magnetic moments: one is the "square" antiferromagnetic component in the plane, and another is the ferromagnetic component along the z axis direction just the same direction as Mn2 atoms. The refined Γ^{5g} moment for Mn atoms at 6 K is 2.68(5) μ_B. For the M-1 phase, the refined "square" antiferromagnetic component moment for Mn3 atoms is 2.18(2) μ_B and the ferromagnetic component moment is 0.7(2) μ_B, while the collinear antiferromagnetic moment is 0.89(7) μ_B for Mn1

and Mn2 at 6 K. The phase coexistent phenomena have also been reported in Mn_3ZnN.[24,25] Generally, the coexistence of the magnetic phases or phase separation behaviors indicates the thermodynamic competition between the phases with nearly identical free energies.[25,35] The triangular Γ^{5g} and tetragonal M-1 magnetic phase in $Mn_3Ga_{0.95}N_{0.94}$ form the nearly identical free energies at ground state inducing their stably coexistence below 50 K.

Figure 2a shows the temperature dependence of magnetization $M(T)$ in the field cooling (FC) way under the selected applied pressures and an external magnetic field of 50 KOe, and presents the magnetic transformation under the (T, H) external fields. Figure 2b shows the extremum of the dM/dT-T curves from 200 to 300 K. Two magnetic transitions can be found with increasing temperature, which is in agreement with the results shown in Figure 1. The corresponding transition temperatures are defined as T_t and T_N, respectively. Furthermore, with increasing pressure, the Neel temperature T_N moves to low temperature and then disappears at 750 MPa. The transition temperature T_t first increases, but then decreases as the Γ^{5g} phase disappears when the pressure increases higher than 750 MPa.

In order to differentiate the specific evolution for each magnetic structure and the spin ordering transformation under external (T, P) fields, the NPD analysis at different temperatures and pressures is carried out, as shown in Figure 2c–f. With increasing pressure, the antiferromagnetic (AFM) ordering temperature T_N decreases and the magnetic transition temperature T_t increases, which is in agreement with the $M–T$ measurements (Figure 2a,b). The temperature range for existence of the Γ^{5g} phase also becomes narrower with increasing pressure, suggesting that the Γ^{5g} magnetic structure is unstable under pressure. As the pressure increasing to 450 MPa, Γ^{5g} phase always stably coexists with the PM phase in the temperature range of 166–175 K. The 180–196 K temperature range under 600 MPa shows a special three-phase coexistence zone of M-1, Γ^{5g}, and PM phases, where the phase fraction for Γ^{5g} phase remains 77.7%, while the M-1 phase fraction increases and the PM phase fraction decreases upon cooling.

From Figure 2, it can be seen that the pressure can enable the phase transition to occur at a higher temperature, e.g., the Γ^{5g} AFM to M-1 ferrimagnetic (FIM) phase transition temperature changes from 100 to 195 K with the pressure increasing from 0 to 750 MPa. Therefore the baromagnetic effect (BME) can be obtained under pressures at certain fixed temperatures, i.e., 130 K. **Figure 3**a indicates the change of the Γ^{5g} AFM to M-1 FIM phase transition temperature with increasing pressure, and Figure 3b shows the macroscopic magnetism measured by SQUID. At 130 K, the macroscopic magnetism changes from 0 μ_B $(f.u.)^{-1}$ at Γ^{5g} AFM phase to 0.63 μ_B $(f.u.)^{-1}$ at M-1 FIM phase under the pressure of 750 MPa.

Next, we will discuss the BME using the $M–T$ curves under increasing pressure with the magnetic field of 50 KOe. The BME can be described by the difference between the magnetic moments at different pressure as represented by the parameter ΔM_p:

$$\Delta M_p = M(T, p) - M(T, p_0) \qquad (1)$$

where p_0 stands for the atmospheric pressure and $M(T, p)$ is the magnetization under thermal and pressure (T, p) fields

with the magnetic field of 50 KOe as shown in Figure 3a. Upon applying different pressure fields, the ΔM_p curves show peaks at 105 K with the external magnetic field of 50 KOe. The maximum ΔM_p with the applied magnetic field 50 KOe is 0.19 μ_B (Mn atom)$^{-1}$, i.e., 0.57 μ_B $(f.u.)^{-1}$ at 105 K and 1000 MPa. Such BME is totally caused by the local ferromagnetic component moments, which could be easily detected from the changes of the interatomic distances. Moreover, the BME for the spontaneous magnetization (M_S) at 130 and 170 K have also been discussed. Based on the isothermal magnetization and Arrott plots under the selected hydrostatic pressures, the M_S data can be obtained by extending the M^2-H/M curve to $H/M = 0$ position,[36] as shown in S3 (Supporting Information). The pressure dependences of M_S at 130 K and 170K are shown in Figure 3b. The M_S for Γ^{5g} AFM phase is zero. The maximum BME for the Γ^{5g} AFM phase to M-1 phase transition is 0.21 μ_B (Mn atom)$^{-1}$, i.e., 0.63 μ_B $(f.u.)^{-1}$ at 130 K with the pressure of 750 MPa, while the distance between Mn atoms (d_{Mn-Mn}) decreases from 2.75845(6) to ≈2.733 Å.

The specific BME obtained at 130 K is accompanied with the decreasing Mn–Mn distance and the magnetic phase transition from the Γ^{5g} phase to the M-1 phase, i.e., the spin re-orientation induced by pressure is shown in **Figure 4**. The path of spin re-orientation from AFM phase to FIM phase is determined by the magnetic structures of the two phases: Γ^{5g} and M-1. The nearly identical free energies at ground state for the two metastable noncollinear magnetic phases indicate that it is easy to cause the phase transition (spin re-orientation) from Γ^{5g} to M-1 by pressure. It is useful to discuss the characteristics of the two magnetic structures to clarify the transformation path of the Mn spin. On the other hand, the hydrostatic pressure induces also the change of another magnetic transition from Γ^{5g} AFM phase to PM state at higher temperature, which is shown in Figure 3c,d and will be discussed for a while. For clarifying the change of the spin orientation by the hydrostatic pressure, Figure 4a illustrates the magnetic order in the (111) plane of the Γ^{5g} magnetic structure, which can clearly display the characteristic of the noncollinear triangular AFM at 130 K without any applied pressure field. The spin orientations of the M-1 magnetic structure are shown in Figure 4b. The (201) plane for the M-1 phase is just the same as the (111) plane in Γ^{5g} phase. However, the directions of the magnetic order in the M-1 phase are not solely in the (201) plane, which means that the spin rotations in the spin re-orientation process do not only occur in the (201) plane, but proceed in a way that some components are out of the (201) plane. The magnetic components in and out of the (201) plane for Mn atoms in the M-1 phase are displayed in Figure 4c. The magnetic moments for Mn1 and Mn2 atoms are the same magnitude but in the opposite direction. The Mn1/Mn2 in Figure 4c is corresponding to Mn1 or Mn2 atom in M-1 magnetic structure. The Mn3 atoms shown "square" antiferromagnetic moment in M-1 magnetic structure have two types of different components in the (201) plane, which are labeled as Mn3-1 and Mn3-2 in Figure 4b. Figure 4d shows the spin re-orientation process for each Mn atoms in the (201) plane with the applied pressure field from 0 to 750 MPa. Under a pressure of 750 MPa, the angles of the spin rotations in (201) plane for Mn1/Mn2, Mn3-1 and Mn3-2 atoms during the spin re-orientation process are 90°, 30°, and ≈45.4°, respectively, accompanied
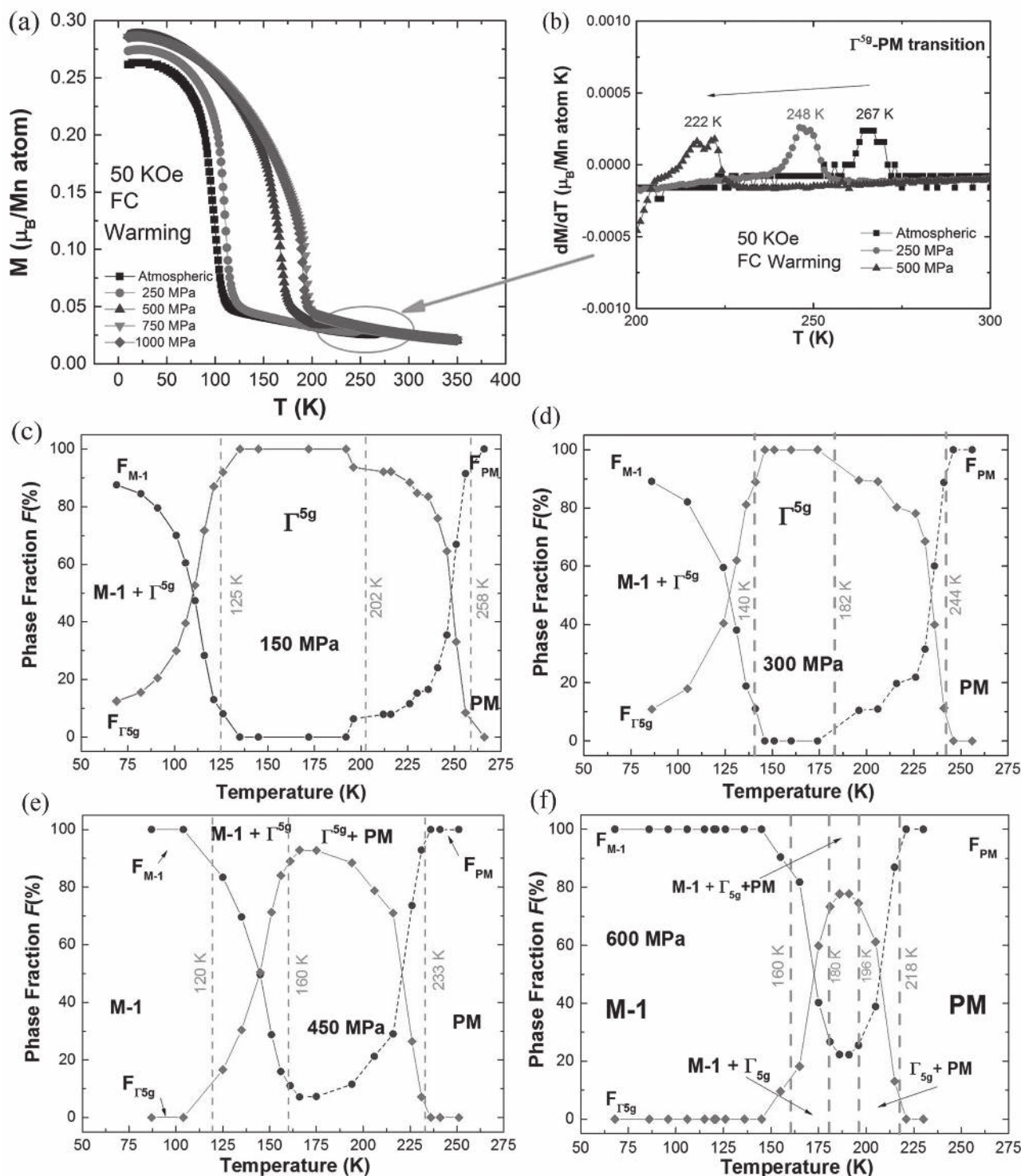
Figure 2. a) Temperature dependence of magnetization (FC) of $Mn_3Ga_{0.95}N_{0.94}$ under selected hydrostatic pressures with external magnetic field of 50 KOe, which shows the obvious magnetic transition from M-1 to Γ^{5g}. b) The extremum of the dM/dT-T curves in the temperature range of 200–300 K, showing the Γ^{5g} - PM transition. c–f) Temperature dependence of the phase fraction for $Mn_3Ga_{0.95}N_{0.94}$ at 150 MPa, 300 MPa, 450 MPa and 600 MPa, respectively. The solid line with circle and rhombus symbols are the phase fractions for M-1 and Γ^{5g} phases, respectively. The dotted lines with circle symbol stands for the phase fraction of PM phase, analyzed from NPD data.

with the Mn–Mn distance decreasing from 2.75845(6) to ≈2.733 Å. On the other hand, although the spin re-orientation can be successfully induced by pressure field, it is difficult to

be produced by magnetic field, because there were no obvious shifts of the magnetic transition temperature with increasing magnetic field from 100 Oe to 50 KOe.
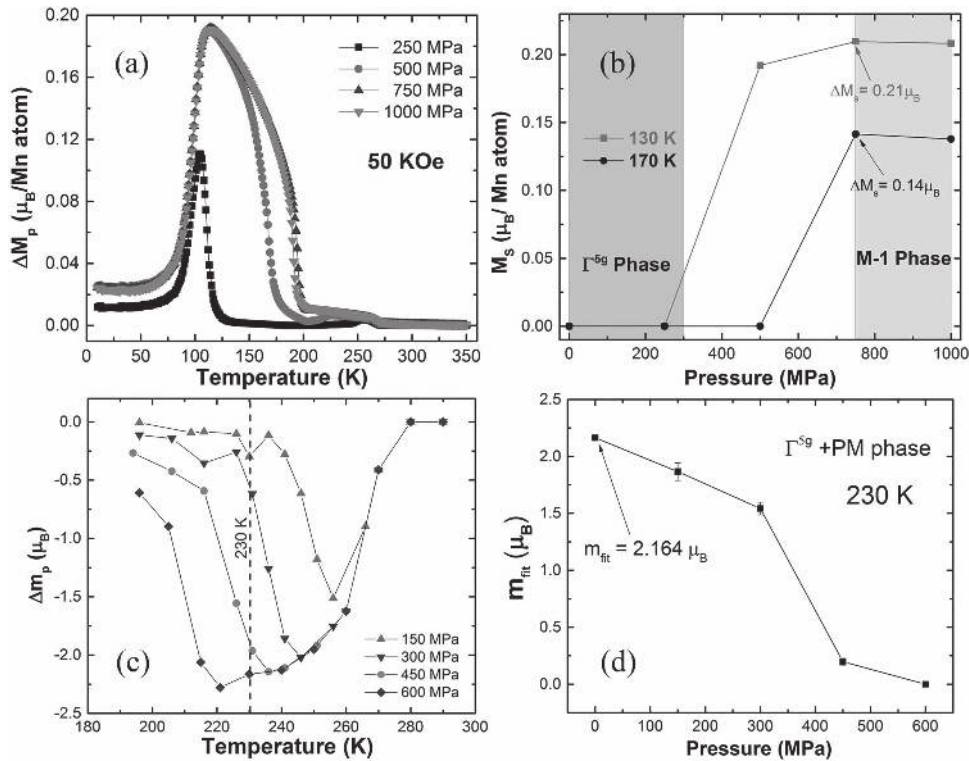
Figure 3. a) Baromagnetic effect (BME) obtained from the *M–T* curve, under the applied hydrostatic pressures with an external magnetic field of 50 KOe. b) Pressure dependence of the spontaneous magnetization at 130 and 170 K. c) Fitted magnetic moment change as a function of temperature, associated with the isothermal application of the hydrostatic pressures (from atmospheric pressure up to the indicated value) for $Mn_3Ga_{0.95}N_{0.94}$. d) Fitted magnetic moment m_{fit} as a function of the applied hydrostatic pressure for Γ^{5g} and PM two-phase coexisting range at 230 K without applying magnetic field.

NPD data also revealed the magnetic moment change upon the pressure-induced magnetic transition from the Γ^{5g} phase to PM phase. The temperature dependence of the fitted magnetic moment m_{fit} from 200 to 290 K at the selected hydrostatic pressures for $Mn_3Ga_{0.95}N_{0.94}$ is shown in S4 (Supporting Information). The pressure-induced difference of the fitted magnetic moment Δm_p shown in Figure 3c can be obtained from the following equation:

$$\Delta m_p = m_{fit}(T, p) - m_{fit}(T, p_0) \qquad (2)$$

The maximum of the pressure-induced fitted magnetic moment change Δm_p under 600 MPa is -2.278 μ_B $(f.u.)^{-1}$ at 220 K for the AFM magnetic transition (from Γ^{5g} phase to PM phase). Figure 3d shows the pressure dependence of the fitted magnetic moment m_{fit} at 230 K. The pressure-induced fitted AFM magnetic moment change for the transition from Γ^{5g} phase to PM phase is -2.164 μ_B $(f.u.)^{-1}$ from 0 to 600 MPa with the d_{Mn-Mn} changing from 2.75784(8) to 2.7380(1) Å.

To fully understand the typical BME mechanism, we focus on the change of Mn–Mn distance and the spin orientation with various pressure fields. As an intermetallic compound, the magnetism change induced by the Mn interatomic distance d_{Mn-Mn} in $Mn_3Ga_{0.95}N_{0.94}$ can be well explained by Ruderman–Kittel–Kasuya–Yosida (RKKY) interaction theory.[37–39] According to the theory, the exchange integral J_{ij} can be expressed as $J_{ij} = -\dfrac{2mk_F^4}{\pi h^2} J_{pd}^2 F(2k_F r_{ij}) \exp(-r_{ij}/l)$, where r_{ij} is the distance between the magnetic atoms at sites i and j.[40] The change of

magnetic atom distance r_{ij} can vary the exchange integral J_{ij}, which results in the magnetism change of the compound. Further change of the magnetic atoms distance d_{Mn-Mn} accompanied with a spin structure change, i.e., spin re-orientation induced by pressure field can lead to a considerable macroscopic magnetic moment change, which is the main cause of the BME obtained in $Mn_3Ga_{0.95}N_{0.94}$ here, as described in Figure 4.

In 2008, a piezomagnetic effect in Mn_3GaN was calculated by Lukashev et al.[32] As a noncollinear antiferromagnetic, the spin rotations easily occur with the application of the strain field, which induces the considerable piezomagnetic effect, i.e., 0.04 μ_B $(f.u.)^{-1}$ at 1% of compressive strain for the Γ^{5g} AFM phase in Mn_3GaN. However, for the whole application process of strain field as predicted, the Γ^{5g} AFM magnetic phase which does not display macroscopic magnetic property is always stably existing under strain field, which is quite different from the BME reported here. The piezomagnetic effect is caused by the spin rotations with the application of an inner strain field in solid lattice, induced probably by lattice distortion or elemental doping. However, the angles for spin rotations are very small and there is no obvious magnetic phase transition in the process. But for BME, the magnetic change is mainly induced by the distance of magnetic atoms decreasing and the spin reorientation under pressure field indicating an obvious magnetic phase transition here. The BME at 130 K for $Mn_3Ga_{0.95}N_{0.94}$ is 0.63 μ_B $(f.u.)^{-1}$ with the pressure field of 750 MPa, i.e., ≈ -9‰ strain change which is nearly 15 times more than the calculated piezomagnetic effect in Mn_3GaN.[32] Moreover, the previous
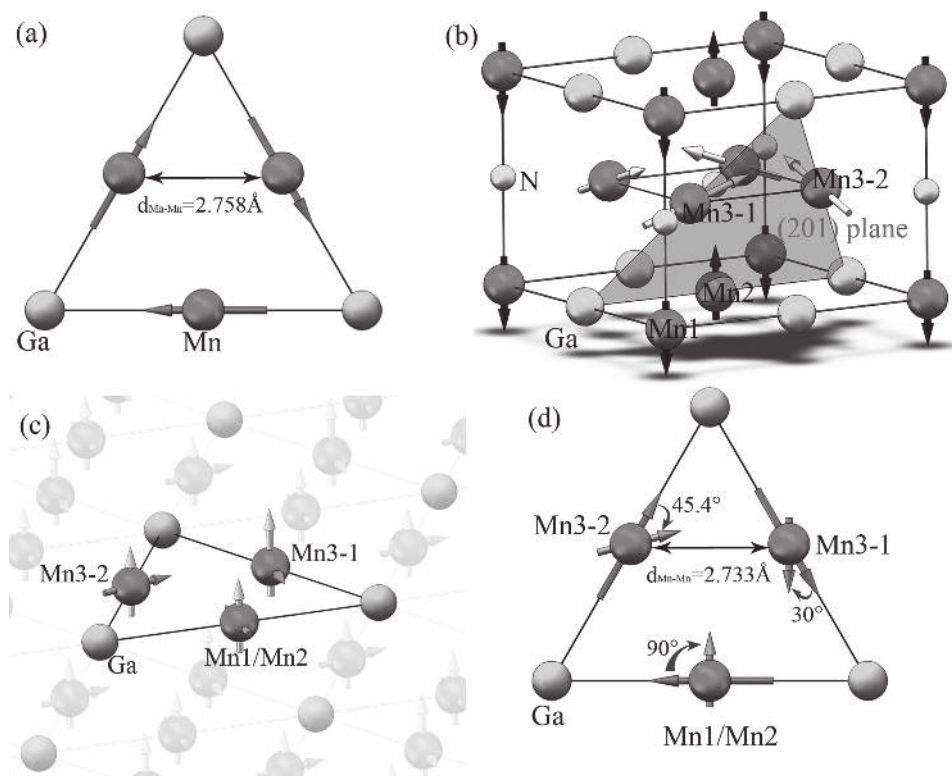
Figure 4. a) Magnetic order on Mn sites in (111) plane of Γ^{5g} AFM structure. The Mn–Mn distance at 130 K under atmospheric pressure is also displayed. b) Magnetic unit cell for M-1 FIM phase. The (201) plane marked with shadow in M-1 structure is just the same as the original (111) plane in the Γ^{5g} structure. The black arrow shows the collinear antiferromagnetic moment of Mn1 and Mn2 atoms, while the gray arrow gives the resultant vector of magnetic order for Mn3 atoms. We separate the Mn3 atoms in (201) plane as Mn3-1 and Mn3-2 atom. c) The magnetic components in the (201) plane (dark arrow) and out of the (201) plane (light arrow) for the M-1 magnetic structure. d) The spin re-orientation in the (201) plane, i.e., (111) plane, from Γ^{5g} to M-1 phase by pressure. The Mn–Mn distance at 130 K under 750 MPa is shown.

work did not predict and consider the occurrence of the M-1 FIM phase, which is just the important factor for the special BME besides the change of the Mn–Mn distance due to the strain by pressure. The pressure-induced spin re-orientation from Γ^{5g} AFM phase to M-1 FIM phase should be primarily responsible for the greater BME observed than the calculated piezomagnetic effect.

In conclusion, the evolution of the magnetic phases under external fields (*T*, *P*) for $Mn_3Ga_{0.95}N_{0.94}$ has been systematically studied. A new FIM magnetic structure M-1 phase is for the first time found in coexistence with the Γ^{5g} AFM phase in the low temperature range of 6–50 K. Correspondingly, a hydrostatic pressure field can modify the existence of M-1, Γ^{5g} and PM phases and induce considerable magnetic phase transitions. As a result, in $Mn_3Ga_{0.95}N_{0.94}$ a large BME with the macroscopically measured value of 0.63 $\mu_B\,(f.u.)^{-1}$ for the Γ^{5g} to M-1 phase transition at 130 K was observed, and a value of −2.164 $\mu_B\,(f.u.)^{-1}$ for the Γ^{5g} to PM phase transition at 230 K under the hydrostatic pressure field was obtained by NPD data analysis. We believe that the BME is the result of the strong coupling effect between the lattice and spin. The pressure introduces the change of Mn–Mn distance and the re-orientation of spin ordering, i.e., magnetic phase transition, thus induces the change of the macroscopic magnetism. Our study opens a new venue toward finding, tuning, and

producing high-level ME intelligent devices and instruments for the future.

Experimental Section

Polycrystalline samples of the nominal composition Mn_3GaN was prepared by a solid-state reaction in vacuum (10^{-5} Pa), using Mn_2N, which was synthesized by sintering Mn powder (4N) in nitrogen gas flow and Ga (4N) as staring materials. Stoichiometric amounts of Mn_2N powder and Ga pellets were mixed and sintered for 2 h in the Ar gas flow. The mixed powder was then pressed into pellets after mechanical grinding, sealed in vacuum in a quartz tube, sintered at 800 °C for several days, and then cooled to room temperature.

Neutron powder diffraction (NPD) data were collected using the BT-1 high-resolution neutron powder diffractometer at NIST Center for Neutron Research (NCNR). A Cu (311) monochromator was used to produce monochromatic neutron beam with wavelength of 1.5403 Å. Neutron diffraction data were collected in the temperature range of 6–300 K. The crystal and magnetic structures were determined by the Rietveld refinement method using the General Structure Analysis System (GSAS) program,[41] where the neutron scattering lengths were used of −0.373, 0.729, and 0.936 ($\times 10^{-12}$ cm) for Mn, Ga, and N, respectively. The pressure effect on the NPD pattern was studied in the BT-1 instrument using an aluminum cell and helium gas as the pressure medium.[42] The magnetic measurements under selected pressure field were carried out using a Quantum Design superconducting quantum interference device (7T-SQUID) magnetometer (10–350 K, 0–70 KOe)

system and hydrostatic pressure cell (easyLab Mcell 10) of Steady High Magnetic Field Facilities (SHMFF) at High Magnetic Field Laboratory, Chinese Academy of Science in Heifei Province. All the tests are obtained by warming processes.

Supporting Information

Supporting Information is available from the Wiley Online Library or from the author.

Acknowledgements

[1] Q. M. Si, S. Rabello, K. Ingersent, J. L. Smith, *Nature* **2001**, *413*, 804.
[2] A. Georges, G. Kotliar, W. Krauth, M. J. Rozenberg, *Rev. Mod. Phys.* **1996**, *68*, 13.
[3] E. Morosan, D. Natelson, A. H. Nevidomskyy, Q. M. Si, *Adv. Mater.* **2012**, *24*, 4896.
[4] J. Ryu, S. Priya, K. Uchino, H. E. Kim, *J. Electroceram.* **2002**, *8*, 107.
[5] V. K. Pecharsky, K. A. Gschneidner Jr., *Phys. Rev. Lett.* **1997**, *78*, 4494.
[6] B. G. Shen, J. R. Sun, F. X. Hu, H. W. Zhang, Z. H. Cheng, *Adv. Mater.* **2009**, *21*, 4545.
[7] O. Tegus, E. Bruck, K. H. J. Buschow, F. R. de Boer, *Nature* **2002**, *415*, 150.
[8] J. F. Lin, H. Watson, G. Vankó, E. E. Alp, V. B. Prakapenka, P. Dera, V. V. Struzhkin, A. Kubo, J. Y. Zhao, C. McCammon, W. J. Evans, *Nat. Geosci.* **2008**, *1*, 688.
[9] J. Badro, J. P. Rueff, G. Vankó, G. Monaco, G. Fiquet, F. Guyot, *Science* **2004**, *305*, 383.
[10] T. Tsuchiya, R. M. Wentzcovitch, C. R. S. da Silva, S. de Gironcoli, *Phys. Rev. Lett.* **2006**, *96*, 198501.
[11] X. Obradors, L. M. Paulius, M. B. Maple, J. B. Torrance, A. I. Nazzal, J. Fontcuberta, X. Granados, *Phys. Rev. B* **1993**, *47*, 12353.
[12] V. Laukhin, J. Fontcuberta, J. L. García-Muñoz, X. Obradors, *Phys. Rev. B* **1997**, *56*, 10009.
[13] M. Imada, A. Fujimori, Y. Tokura, *Rev. Mod. Phys.* **1998**, *70*, 1039.
[14] H. Ogasawara, A. Kotani, *Phys. Rev. B* **2000**, *62*, 7970.
[15] A. Kotani, S. Shin, *Rev. Mod. Phys.* **2001**, *73*, 203.
[16] S. Medvedev, T. M. McQueen, I. A. Troyan, T. Palasyuk, M. I. Eremets, R. J. Cava, S. Naghavi, F. Casper, V. Ksenofontov, G. Wortmann, C. Felser, *Nat. Mater.* **2009**, *8*, 630.
[17] M. K. Wu, J. R. Ashburn, C. J. Torng, *Phys. Rev. Lett.* **1987**, *58*, 908.
[18] L. Mañosa, D. G. Alonso, A. Planes, E. Bonnot, M. Barrio, J. L. Tamarit, S. Aksoy, M. Acet, *Nat. Mater.* **2010**, *9*, 478.
[19] L. Mañosa, D. G. Alonso, A. Planes, M. Barrio, J. L. Tamarit, I. S. Titov, M. Acet, A. Bhattacharyya, S. Majumdar, *Nat. Commun.* **2011**, *2*, 595.
[20] E. J. R. Plaza, J. C. P. Campoy, *Phys. Rev. B* **2007**, *75*, 174419.
[21] K. Takenaka, H. Takagi, *Appl. Phys. Lett.* **2005**, *87*, 261902.
[22] X. Y. Song, Z. H. Sun, Q. Z. Huang, M. Rettenmayr, X. M. Liu, M. Seyring, G. N. Li, G. H. Rao, F. X. Yin, *Adv. Mater.* **2011**, *23*, 4690.
[23] S. H. Deng, Y. Sun, H. Wu, Q. Z. Huang, J. Yan, K. W. Shi, M. I. Malik, H. Q. Lu, L. Wang, R. J. Huang, L. F. Li, C. Wang, *Chem. Mater.* **2015**, *27*, 2495.
[24] C. Wang, L. H. Chu, Q. R. Yao, Y. Sun, M. M. Wu, L. Ding, J. Yan, Y. Y. Na, W. H. Tang, G. N. Li, Q. Z. Huang, J. W. Lynn, *Phys. Rev. B* **2012**, *85*, 220103.
[25] Y. Sun, C. Wang, Q. Z. Huang, Y. F. Guo, L. H. Chu, M. Arai, K. Yamaura, *Inorg. Chem.* **2012**, *51*, 7232.
[26] Y. Sun, C. Wang, L. H. Chu, Y. C. Wen, M. Nie, F. S. Liu, *Scripta Mater.* **2010**, *62*, 686.
[27] L. Ding, C. Wang, L. H. Chu, J. Yan, Y. Y. Na, Q. Z. Huang, X. L. Chen, *Appl. Phys. Lett.* **2011**, *99*, 251905.
[28] K. Asano, K. Koyama, K. Takenaka, *Appl. Phys. Lett.* **2008**, *92*, 161909.
[29] J. Yan, Y. Sun, H. Wu, Q. Z. Huang, C. Wang, Z. X. Shi, S. H. Deng, K. W. Shi, H. Q. Lu, L. H. Chu, *Acta Mater.* **2014**, *74*, 58.
[30] E. F. Bertaut, D. Fruchart, J. P. Bouchaud, R. Fruchart, *Solid State Commun.* **1968**, *6*, 251.
[31] D. Matsunami, A. Fujita, K. Takenaka, M. Kano, *Nat. Mater.* **2015**, *14*, 73.
[32] P. Lukashev, R. F. Sabirianov, K. Belashchenko, *Phys. Rev. B* **2008**, *78*, 184414.
[33] K. Y. Kim, K. T. Byun, H. Y. Kwak, *Chem. Eng. J.* **2007**, *132*, 125.
[34] D. Fruchart, E. F. Bertaut, *J. Phys. Soc. Jpn.* **1978**, *44*, 781.
[35] E. Granado, Q. Huang, J. W. Lynn, J. Gopalakrishnan, R. L. Greene, K. Ramesha, *Phys. Rev. B* **2002**, *66*, 064409.
[36] W. Li, R. J. Huang, W. Wang, J. Tan, Y. Q. Zhao, S. P. Li, C. J. Huang, J. Shen, L. F. Li, *Inorg. Chem.* **2014**, *53*, 5869.
[37] M. A. Ruderman, C. Kittel, *Phys. Rev.* **1954**, *96*, 99.
[38] K. Yosida, *Phys. Rev.* **1957**, *106*, 893.
[39] T. Kasuya, *Prog. Theor. Phys.* **1956**, *16*, 45.
[40] F. Matsukura, H. Ohno, A. Shen, Y. Sugawara, *Phys. Rev. B* **1998**, *57*, 2037.
[41] A. C. Larson, R. B. van Dreele, *General Structure Analysis System (GSAS)*, Los Alamos National Laboratory Report, Los Alamos **2004**.
[42] C. R. dela Cruza, B. Lorenza, W. Ratcliffb, J. Lynnb, M. M. Gospodinovc, C. W. Chua, *Physica B* **2008**, *403*, 1359.